LANGMUIR

pubs.acs.org/Langmuir Article

# Microdome-Induced Strain Localization for Biaxial Strain Decoupling toward Stretchable and Wearable Human Motion Detection

Min Seong Kim, Kyuyoung Kim, Donguk Kwon, Seunghwan Kim, Jimin Gu, Yong Suk Oh,* and Inkyu Park*

Cite This: *Langmuir* 2020, 36, 8939–8946 Read Online

ACCESS | Metrics & More | Article Recommendations | Supporting Information

**ABSTRACT:** Soft strain sensors have attracted significant attention in wearable human motion monitoring applications. However, there is still a huge challenge for decoupled measurement of multidirectional strains. In this study, we have developed a biaxial and stretchable strain sensor based on a carbon nanotube (CNT) film and a microdome array (MA)-patterned elastomeric substrate. The MA structures lead to generating localized and directional microcracks of CNT films within the intended regions under tensile strain. This mechanism allows a single sensing layer to act as a strain sensor capable of decoupling the biaxial strains into axial and transverse terms. The ratio of resistance change between two perpendicular axes is about 960% under an *x*-directional strain of 30%, demonstrating the biaxial decoupling capability. Also, the proposed strain sensor shows high stretchability and excellent long-term reliability under a cyclic loading test. Finally, wearable devices integrated with the strain sensor have been successfully utilized to monitor various human motions of the wrist, elbow, knee, and fingers by measuring joint bending and skin elongation.

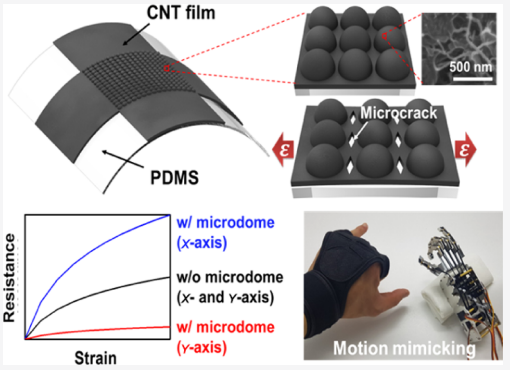


## INTRODUCTION

Strain sensors have attracted tremendous attention in a variety of applications, including personal health care,[1] prosthetics,[2,3] smart clothes,[4,5] and robotics.[6,7] Especially, wearable strain sensors with large stretchability, broad sensing range, and high sensitivity are desirable for human motion detection. However, conventional strain sensors based on metals or semiconductors exhibit a low sensitivity and a narrow sensing range (<5%). As an alternative solution, conductive nanomaterials such as carbon nanotubes (CNTs),[8−13] graphene,[14−16] metallic nanowires,[17−20] and nanoparticles[21−24] have been incorporated into a polymer matrix for the fabrication of soft strain sensors.

Thus far, the development of soft strain sensors has been mainly focused on the improvement of sensitivity, stretchability, response speed, or dynamic range. However, one of the paramount issues in practical motion detection applications is the decoupling capability of multiaxial motions. In order to resolve this issue, complicated multilayer structures[25−28] or signal processing techniques[29] have been introduced. Ryu et al.[25] suggested a soft strain sensor based on the CNT fibers and Ecoflex, which showed high stretchability and sensitivity with multiaxial strain detection capability. In this report, highly oriented dry-spun CNT fibers were deposited on the prestrained Ecoflex substrate and exhibited a constant decrease of the resistance over 900% of strain. They stacked the sensing layers heading different directions for the multiaxial strain detection. In the other approach, Gou et al.[28] reported highly sensitive and long-term durable soft strain sensors fabricated by programmed direct printing of the CNTs on a polydimethylsiloxane (PDMS) substrate. The sensitivity of the sensor was tuned by controlling the printing cycles of the CNTs, and the multiaxial sensing capability was derived from a rosette-type sensor array. Kim et al.[29] proposed a CNT−Ecoflex nanocomposite-based soft strain sensor fabricated by a three-dimensional (3D) injection molding process. They introduced an anisotropic electrical impedance tomography method to realize a multipoint strain mapping. Although various arrangements of CNT−polymer layers or complicated signal processing facilitated the multiaxial strain sensing, they suffered from a low-throughput, time-consuming, complicated fabrication process and additional circuit systems. Namely, it has been difficult for a single active layer of CNT-based strain sensors to decouple strains in axial and transverse directions by

**Received:** May 16, 2020
**Revised:** June 30, 2020
**Published:** July 2, 2020

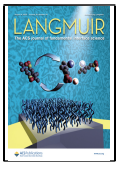







https://dx.doi.org/10.1021/acs.langmuir.0c01450
*Langmuir* 2020, 36, 8939−8946

their fundamental sensing mechanism based on the disconnection of percolation networks of the CNTs.

Here, we propose a microcrack-controlled (MC) stretchable strain sensor capable of biaxial strain sensing by introducing a microdome array (MA) to an elastomeric substrate having CNT percolation networks on its surface. Because the microcracks are directionally generated only at intended regions of the CNT film because of the MA structures, this strain sensor can simultaneously detect the biaxial strains, that is, the direction and amplitude of strains in two axes independently. The biaxial sensing capability is successfully achieved using a single active layer without any complicated circuitry. In addition, we have verified high stretchability and long-term reliability of the sensor. Finally, we demonstrate that the MC strain sensor can be utilized as a wearable device for measuring various human motions.

## RESULTS AND DISCUSSION

Figure 1a(i) shows a schematic illustration of the MC strain sensor, which consists of a microstructured PDMS substrate and a spray-coated CNT film. The inset shows a scanning electron microscopy (SEM) image of the CNTs forming 3D percolation networks as an active sensing element. The MA-patterned PDMS substrate provides a local strain concentration on the CNT layer as well as stretchability. In Figure 1a(ii), the microcracks of the CNT film are opened upon prestretching only at a specific area because of the MA structures. After releasing, the microcracks are closed reversibly.

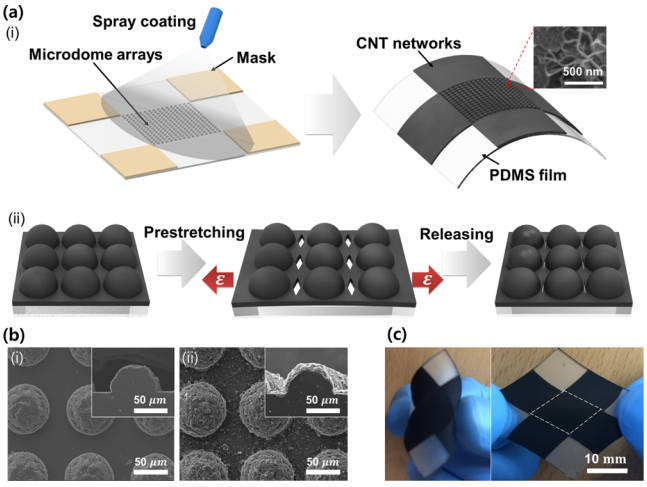


**Figure 1.** Structure of an MC strain sensor: (a) (i) schematic illustration of the MC strain sensor that consists of an MA-patterned PDMS substrate and a CNT film fabricated using spray coating. The inset shows an SEM image of CNTs forming 3D percolation networks. (ii) Microcracks of the CNT film are opened at a specific area upon prestretching and closed after releasing. (b) SEM images of the top and cross-sectional view of the MA-patterned PDMS substrate (i) before and (ii) after CNT spray coating. (c) Photographic images of the MC strain sensor under bending and stretching. MA structures as a sensing layer are generated in the white-dotted area.

Figure S1 (Supporting Information) shows a schematic illustration of the overall fabrication processes of the MC strain sensor. The fabrication of an MC strain sensor was done by the following process: (i) photoresist patterning on silicon (Si) wafer using photolithography; (ii) Cr mask formation with hole array by electron beam evaporation and lift-off process; (iii) isotropic etching of Si by reactive ion etching (RIE) with a specific composition of reactive gases;[30] (iv) PDMS molding and demolding after coating $C_4F_8$ as an antiadhesion layer[31] (details are provided in the Experimental Section); and (v) CNT networks as a sensing layer were formed using a spray coating method on the surface of the MA-structured PDMS substrate. The thickness of the coated CNT film was controlled by varying the number of spraying, while fixing the spraying distance, pressure, and solution concentration identical. As the CNT film became thicker, the sheet resistance decreased, as shown in Figure S2. However, after 60−70 times of spray coating, the sheet resistance of the MC strain sensor showed a saturated value of 1.3 kΩ/sq. As the spray-coated CNTs form a loosely packed film, the sheet resistance of the CNT networks cannot be further decreased but show a saturation. This phenomenon comes from a limited effective depth of the CNT percolation networks formed by spray coating, which has a relatively deficient film density compared with other metallic films formed by general deposition methods such as evaporation and sputtering.[32]

In Figure 1b, the SEM images show a top surface and a cross section of the MA-patterned PDMS substrate before and after the formation of the CNT percolation networks. The rough surface of the MA-patterned PDMS substrate originates from the dome-shaped Si master mold generated by the RIE process. The spray-coated CNTs were conformally covered and formed as a 3D percolation network on the top surface of the PDMS substrate. Finally, the photographic images of the fabricated sensors under bending and stretching are shown in Figure 1c.

Crack generation of the CNT film originates from the different mechanical properties between the CNT networks and the PDMS substrate upon stretching. Generally, randomly distributed cracks are generated on thin-film-coated flexible substrates under stretching, as illustrated in Figure S3. On the other hand, the MC strain sensor leads to generating directional microcracks within the confined regions by the design for the strain localization. Figure 2a shows a schematic illustration of the decoupling mechanism of the MC strain sensor. As the opening and closing of the microcracks occur along the *y*-axis at intended regions between the MA structures under uniaxial stretching in the *x*-axis direction, the electrical current along the *y*-axis direction is not significantly hindered by the crack generation. Also, the MA structures under biaxial stretching facilitate the formation of directional microcracks, which interrupts the electrical current along the two perpendicular directions, as shown in Figure 2a(ii). The generation of local and directional microcracks arranged with regular intervals is capable of decoupling the biaxial strains into two independent components for each direction.

The strain concentration within confined regions between the MA structures was verified using a finite element method simulation under uniaxial and biaxial strains. Figure 2b shows the von-Mises stress distribution on the CNT film at 5% of tensile strain applied in the *x*-axis direction (i.e., uniaxial strain; Figure 2b(i)) and the two perpendicular directions (i.e., biaxial strains; Figure 2b(ii)). The von-Mises stress within the confined regions showed about 20 times more than that obtained on the hemispherical top of the microdome under both uniaxial and biaxial strains. The *x*-directional strains of the CNT film under applied uniaxial and biaxial loadings were calculated using numerical simulation. The maximum local


https://dx.doi.org/10.1021/acs.langmuir.0c01450
Langmuir 2020, 36, 8939−8946

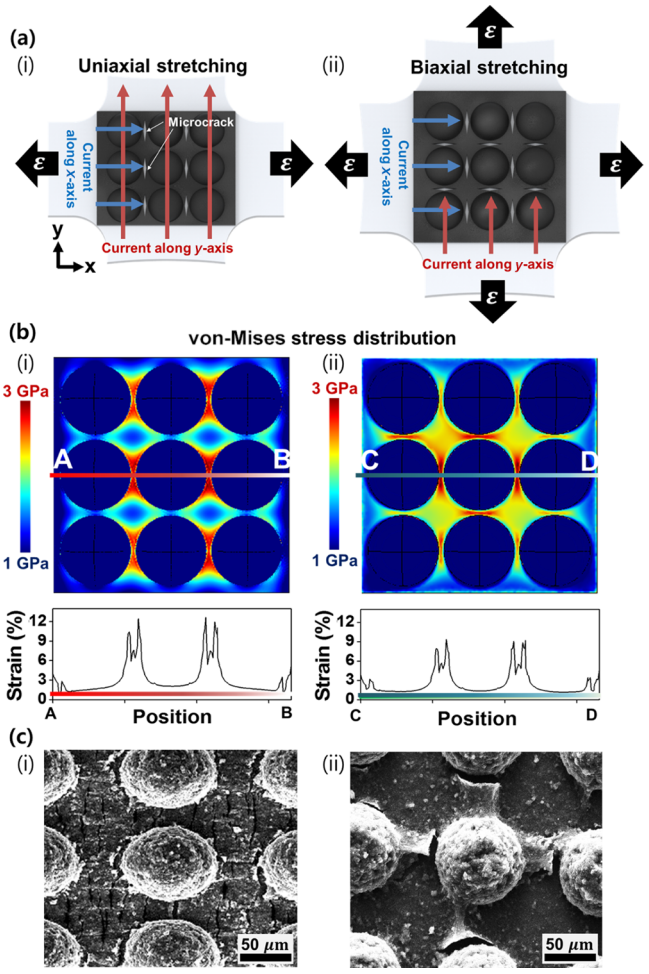


**Figure 2.** Strain sensing mechanism: (a) schematic illustration of (i) uniaxial and (ii) biaxial sensing mechanism derived from the directional microcrack generated within the intended regions between the MA structures. (b) von-Mises stress distribution shows a local stress concentration between the MA structures under 5% of (i) uniaxial and (ii) biaxial strains. Strain distributions were shown under 5% of uniaxial strain and biaxial strains according to the AB and CD lines, respectively. (c) SEM images show the surface of the CNT film coated on the MA-patterned PDMS substrate at (i) uniaxial strain and (ii) biaxial strains.

strain in the confined regions (i.e., between microdomes) reached $\varepsilon_x$ = 12.5%, which is about 2.5 times higher than the global strain in the case of uniaxial loading. Also, the maximum local strain under the biaxial loading was calculated as $\varepsilon_x$ = 9%, which is smaller than that for uniaxial stretching due to the Poisson effect.

Figure 2c shows the SEM images of the top surface of the CNT film coated on the MA-patterned PDMS substrate under 15% of uniaxial and biaxial strains. In Figure 2c(i), the SEM image shows the directional microcracks locally generated along the *y*-axis at the intended regions under uniaxial stretching. In Figure 2c(ii), the SEM image shows the directional microcracks locally generated at the confined regions along the two perpendicular directions under biaxial stretching. Although the microcracks were formed along two perpendicular directions, they did not lead to mechanical fracture or failure of the CNT film/PDMS substrate because of the existence of the microdome. In Figure S4, a quantitative analysis was conducted by comparing the experimental results with the numerical simulation to evaluate the stress concentration-based crack localization behavior. The colorful contour in Figure S4a represents the stress distribution over the CNT film under 10% of the *x*-axis directional strain. Figure S4b shows the calculated values of the *x*-directional strain ($\varepsilon_x$) and the *y*-directional strain ($\varepsilon_y$) along the AB and CD lines. Interestingly, the compressive strain along the CD line reaches −10% because of the Poisson effect. The SEM image in Figure S4c shows the microcrack generation between the microdomes at 20% of uniaxial strain in the *x*-axis direction. A distance between the microdomes increased from 25 to 40 $\mu$m along the *x*-axis direction, while it decreased from 25 to 22 $\mu$m along the *y*-axis direction. In Figure S5, the strain concentration of the CNT layer could be controlled by tuning the size and spacing of the MA arrangement in accordance with the simulation results. It is obvious that the sensitivity of the MC strain sensor increased with strain concentration. This means that the electrical and mechanical properties on the MC strain sensor can be easily tuned by the arrangement design of the MA structures.

The performance of the MC strain sensor was evaluated by experimental analysis. In Figure 3a, the MC strain sensor exhibits an excellent long-term reliability under 25,000 cycles of repeated tensile strains from 10 to 30% with a strain rate of 0.2/s. The inset shows a photographic image of the electromechanical testing system of the MC strain sensor. During 3000 cycles of loading, there was a slight drift in the base resistance, which can be attributed to the stabilization of the crack opening−closing process and a stress relaxation behavior of the elastomeric substrate.[10,23] However, the amplitudes of the resistance changes remained constant after 3000 cycles of loading. In Figure S6, SEM images show the CNT film on the surface of the MC strain sensor after 100,000 cyclic loading with 50% of tensile strain. The CNT layer was not delaminated and still exhibited the electromechanical stability because of an intrinsic stretchability of the CNT networks and the PDMS substrate.

In Figure 3b, the current−voltage ($I$−$V$) characteristics of the MC strain sensor (spacing between microdomes = 5 $\mu$m) show a typical ohmic resistance behavior. The slope of the $I$−$V$ curve representing the base conductance of the sensor decreased as the applied strain increased from 0 to 40%. The inset shows a normalized resistance change ($\Delta R/R_0$) of the MC strain sensor having 5 $\mu$m of spacings between the microdomes with respect to the applied strain. The results include a relationship between the sensitivity of the strain sensor and the number of spraying CNT ($n$) that determines the thickness of the CNT layer. The sensitivity $[(\Delta R/R_0)/\varepsilon]$ of the MC strain sensors is strongly dependent on the thickness of the CNT film layer that acts as an active element. The strain sensor with a thinner CNT layer exhibited higher sensitivity because the thin CNT percolation film shows much higher crack density than those of the thicker case.[33] Also, the signal-to-noise ratio (SNR) of the MC strain sensor was calculated at different ranges of strain, as shown in Figure S7. The SNR value of the MC strain sensor increased from 38.4 to 85.86 dB at a strain ranging from 0.5 to 50%. The high values of SNR enable the MC strain sensor to sufficiently distinguish sensing signals from its noise level even at a small strain range ($\varepsilon$ = 0.5%).

Figure 3c shows $\Delta R/R_0$ of the MC strain sensor with different spacings between microdomes for applied tensile strains. The CNT network on a flat PDMS substrate was used


https://dx.doi.org/10.1021/acs.langmuir.0c01450
Langmuir 2020, 36, 8939−8946

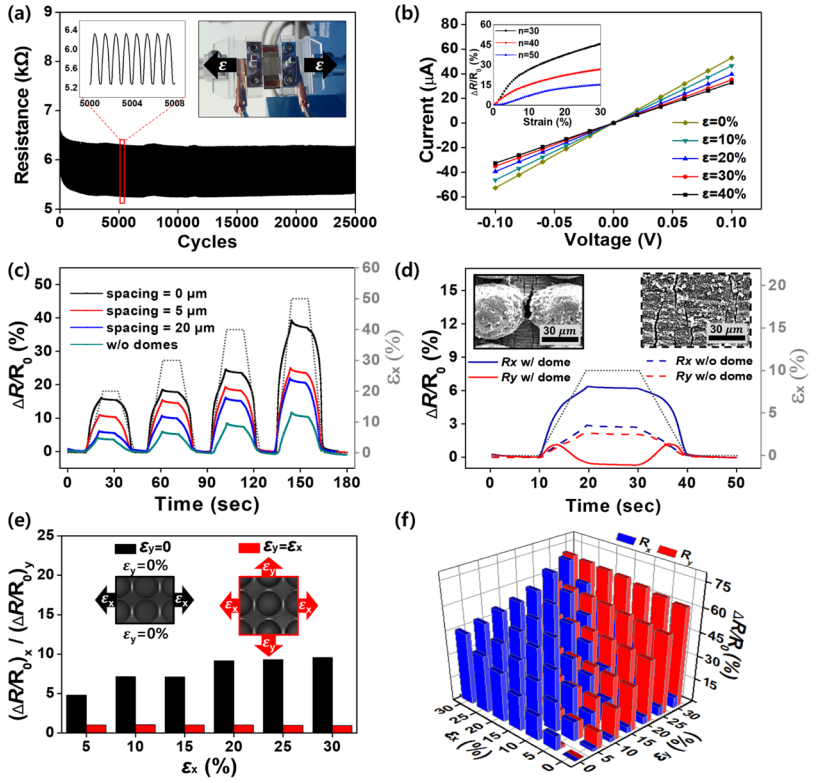


**Figure 3.** Characterization of the MC strain sensor: (a) reliability test under 25,000 cyclic loading from 10 to 30% of tensile strain. The inset photographic image shows the electromechanical testing system. (b) $I-V$ curves of the MC strain sensor having 5 $\mu$m spacing of MA at the different values of strain ranging from 0 to 40%. The inset shows $\Delta R/R_0$ of the MC strain sensors with different thicknesses of the CNT layer ($n$ is the number of CNT spraying). (c) $\Delta R/R_0$ of the MC strain sensors with different spacings under dynamic strains ranging from 20 to 50%. (d) Effect of microdome existence on the responses in $x$- and $y$-directions under the $x$-directional loading situation ($\varepsilon_x$ = 10%). The inset shows the SEM images of the microcracks generated with and without the MA structures. (e) Quantitative comparison of $(\Delta R/R_0)_x/(\Delta R/R_0)_y$ at different uniaxial strains and biaxial strains, respectively. (f) $\Delta R/R_0$ at different biaxial strains ($\varepsilon_x$ and $\varepsilon_y$) ranging from 0 to 30%.

as a reference. The dome diameter was 70 $\mu$m and remained constant, and the dome-to-dome spacing varied from 0 to 5 and 20 $\mu$m. When the tensile strain increased from 20 to 50%, $\Delta R/R_0$ of the MC strain sensor increased with an opening of the CNT microcracks. Also, as the spacing between the microdomes became smaller, the MC strain sensor showed more sensitive response because of an enhanced stress concentration as explained above.

Figure 3d shows $\Delta R/R_0$ in the $x$- and $y$-axis directions of the MC strain sensors with and without MA structures under 10% of $x$-directional strain ($\varepsilon_x$), respectively. In the case of a strain sensor without microdome structures, the magnitude of $\Delta R/R_0$ showed similar and relatively low values of 2−3% for both $x$-axis and $y$-axis directions. This means that randomly distributed microcracks generated by $x$-directional strain interrupt the electrical current even in the $y$-axis direction. On the other hand, the MC strain sensor showed a relatively higher value of $\Delta R/R_0$, 6%, in the $x$-axis direction and a negative $\Delta R/R_0$ value, −0.8%, in the $y$-axis direction. The reason why the resistance of $y$-axis almost maintained for the $x$-directional strain was that the cracks were only generated in the selective regions between the MA along the $y$-axis because of the stress concentration, not in the random region, and electrical current along the $y$-axis direction was not hindered by the cracks, as described in Figure 2a. When it was stretched to more than 8% in the $x$-axis direction, the compressively concentrated strain in the transverse direction led to decreasing $\Delta R/R_0$ in the $y$-axis direction because of the Poisson effect. This phenomenon of compressive strain concentration was confirmed using a numerical simulation, as mentioned in Figure S4.

In Figure 3e, the MC strain sensors were quantitatively evaluated for the biaxial sensing characteristic using a ratio of $\Delta R/R_0$ in the $x$- and $y$-axis directions, defined as $(\Delta R/R_0)_x/(\Delta R/R_0)_y$. $(\Delta R/R_0)_x/(\Delta R/R_0)_y$ showing values close to 1 at $\varepsilon_x = \varepsilon_y$. On the other hand, when only $\varepsilon_x$ increased to 30% at a fixed $\varepsilon_y$ = 0%, $(\Delta R/R_0)_x/(\Delta R/R_0)_y$ gradually increased showing much higher values up to 9.6. These independent responses of the two axes reveal an excellent decoupling characteristic of the MC strain sensor.

In Figure 3f, $\Delta R/R_0$ in the $x$- and $y$-axis directions was compared under biaxial tensile strains within 30% for a decoupling evaluation of the MC strain sensors. The MC strain sensors showed a significant increase of $(\Delta R/R_0)_y$ with $\varepsilon_y$, but a very small increase with $\varepsilon_x$. Especially, $(\Delta R/R_0)_y$ at $\varepsilon_y$ = 30% and $\varepsilon_x$ = 0% showed 13 times larger than that obtained at $\varepsilon_y$ = 0% and $\varepsilon_x$ = 30%. The simple plane fitting of $(\Delta R/R_0)_x$ and $(\Delta R/R_0)_y$ with respect to the biaxial strains showed a strong linear relationship with high R-square values of 0.98 and 0.99, respectively, as explained in Figure S7. This result indicates that both $x$- and $y$-directional strains can be easily predicted from the linear relationship between the strain and $\Delta R/R_0$

In Figure 4a, a schematic diagram shows a MC strain sensor platform covered with a protection cap to fabricate wearable devices for human motion detection. First, a joint band integrated with the strain sensor platform was demonstrated.


https://dx.doi.org/10.1021/acs.langmuir.0c01450
Langmuir 2020, 36, 8939−8946

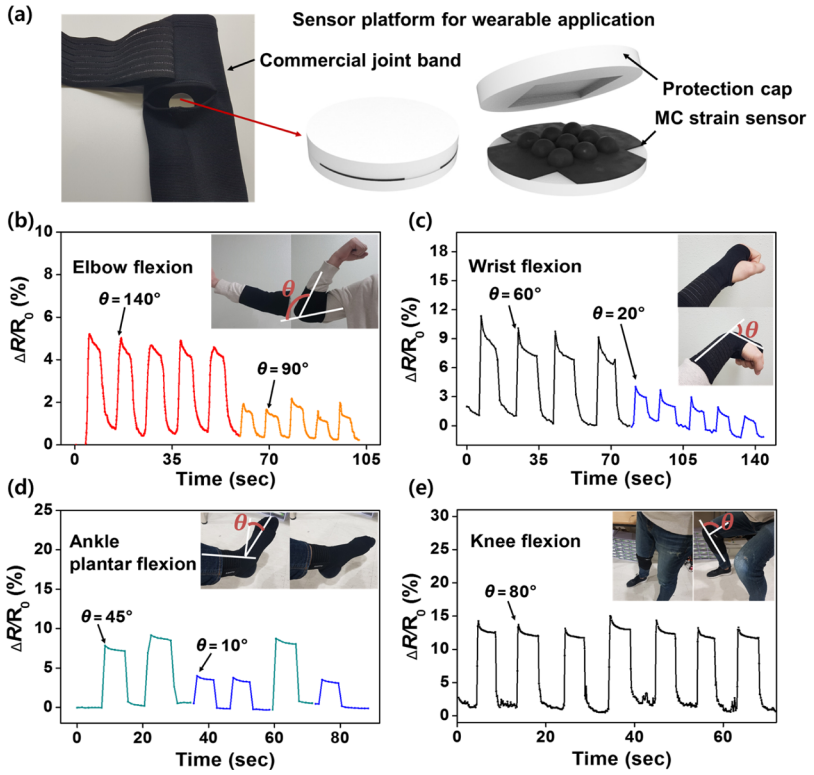


**Figure 4.** Wearable human motion sensing applications of the MC strain sensor: (a) photographic image and schematic illustration of the MC strain sensor platform for wearable applications. Sensing performances of the sensor-integrated joint band under the flexion motions at different angles of the (b) wrist, (c) elbow, (d) ankle, and (e) knee joints.

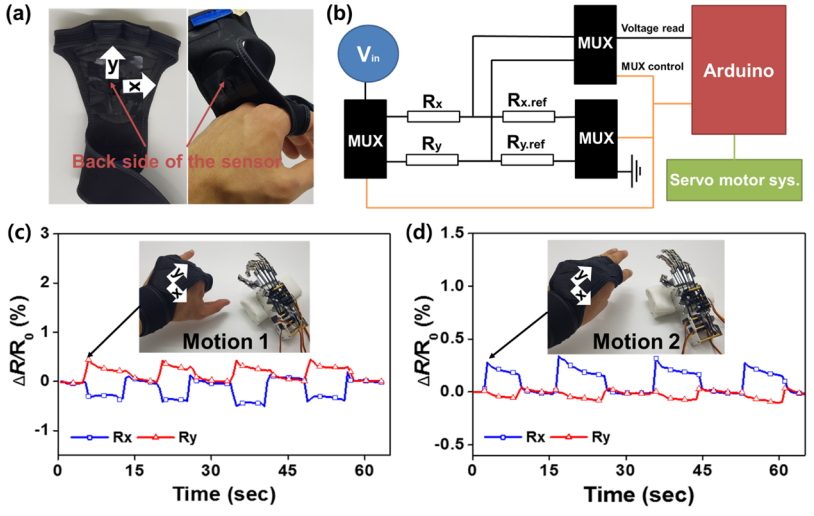


**Figure 5.** Application of the MC strain sensor to a smart glove system and robot control: (a) photographic images of the smart glove capable of monitoring biaxial strains applied on the backside of the human hand and controlling of a robot hand. (b) Circuit diagram of the robot hand control system using the smart glove. (c,d) Biaxial responses of the MC strain sensor attached to the smart glove under different hand motions and corresponding movements of the robot hand that mimic the human hand motions.

In Figure 4b–e, $\Delta R/R_0$ of the strain sensor applied on the joint band was evaluated under repeated flexion–extension motions of wrist, elbow, knee, and ankle, respectively. The results show that the joint bands can accurately detect joint motions at different angles of flexion. In the case of ankle, $\Delta R/R_0$ of the joint band increases with larger plantar flexion angle of the joint motions (Video S1). In Figure 4e, because the joint band mounted on the knee joint underwent a large elongation during repeated squat motion, it showed larger $\Delta R/R_0$ (over 10%) than those obtained from the wrist, elbow, and ankle joints.[34,35] These results represent that the joint band with the MC strain senor is capable of accurately detecting relatively small motions of elbow, wrist, and ankle joints but also exhibiting the excellent durability under the large motions of knee joint.

Figure 5a shows a photographic image of a smart glove integrated with an MC strain sensor. The smart glove is capable of detecting a small biaxial elongation of skin by the


https://dx.doi.org/10.1021/acs.langmuir.0c01450
Langmuir 2020, 36, 8939–8946

crack opening−closing process of the mounted sensor. Figure 5b depicts a circuit diagram of the robot hand control system using an Arduino platform. The sensing output was measured by a voltage-divider circuit, and three multiplexers were utilized to make a multisignal switching system. Figure 5c,d shows the sensing performance and a robot control capability according to two different hand motions. Motion 1 represents the simultaneous bending motions of the index, middle, and ring fingers, and motion 2 is the simultaneous bending motions of the thumb and little finger. The smart glove showed an increase of $(\Delta R/R_0)_y$ under the skin elongation along the $y$-axis in the case of motion 1. It also exhibited a reduction of $(\Delta R/R_0)_x$ due to the compressive strain perpendicular to the direction of elongation. During motion 2, $(\Delta R/R_0)_x$ of the smart glove increased as the back skin of the hand stretched along the $x$-axis direction. However, a less amount of $(\Delta R/R_0)_y$ declined because the skin underwent relatively small compressive strain along the straightforward direction of the middle finger (i.e., $y$-axis direction) under motion 2. These results confirm that the smart glove facilitates the detection of small biaxial strains applied on the backside of the hand generated from different finger motions and that the MC strain sensor can be utilized to detect a small strain over a wide range for wearable applications, that is, detection of the skin elongation with small strains as well as the joint flexion−extension motions with large strains.

Finally, we demonstrated a robot hand control system using the smart glove integrated with the MC strain sensor. The fingers of the robot hand were actuated on a simple tendon-driven system with five servo motors, which were controlled using the voltage outputs from the MC strain sensor. The thumb and little fingers of the robot were controlled by the $x$-directional responses of the smart glove. The servo motors connected to the two robotic fingers were actuated by mapping the value of $(\Delta R/R_0)_x$ of the MC strain sensor during motion 1. In a similar manner, the $y$-directional responses of the sensor were used to actuate the index, middle, and ring fingers of the robot hands. As a result, the robotic fingers successfully mimicked the human finger motions as shown in the inset photographic images of Figure 5c,d and Video S2.

## CONCLUSIONS

In summary, we developed a stretchable MC strain sensor having a biaxial sensing characteristic by introducing a MA-patterned elastomeric substrate and CNT percolation networks. As MA structures were fabricated on the surface of the elastomeric substrate, microcracks of the CNT networks were locally and directionally generated on intended regions between microdomes. The stress concentration-induced localization of microcracks allows the strain sensor to enhance the sensitivity and biaxial sensing characteristic derived by a maximized difference of responses in the two perpendicular directions. Also, the MC strain sensors showed the long-term stability and wide ranges of detection. The MC strain sensor can be utilized for the human motion detection that requires the sensing capability to accurately detect not only small strains arising from the skin but also large strains applied at the joints of the wrist, elbow, and knee. We believe that the stretchable MC strain sensors exhibit a promising potential in human motion applications, including prosthetics, sport dynamics, and personal health care.

## EXPERIMENTAL SECTION

**Preparation of MA-Patterned Master Molds.** A silicon master template for elastomer molding was prepared by serial processes of microfabrication. Photoresist (AZ 5214-E, AZ Electronic Materials, Luxembourg) was patterned in the shape of dot array by conventional photolithography. Cr layer (500 nm) as a mask for performing etching process was deposited on the wafer and the predeposited PR was removed by acetone, the so called lift-off process. Next, the silicon was etched isotropically by RIE with a specific ratio of gas mixture ($O_2$/$SF_6$: 12.5:50 sccm). The plasma power and operating pressure were 100 W and 210 mTorr, respectively. Finally, the Cr layer was stripped by an etchant (Cr-7, Cyantek Corp., USA), resulting in a silicon wafer with an array of hemispherical trenches.

**Fabrication of MC Stretchable Strain Sensors.** Fluorocarbon ($C_4F_8$) was coated on the surface of the prepared silicon mold for easy detachment of a silicone elastomer. PDMS prepolymer and curing agent (Sylgard 184, Dow Corning Inc., USA) were mixed at a ratio of 10:1. After the degassing process, the PDMS mixture was poured on the Si master mold and cross-linked by heating at 80 °C for 2 h. Multiwalled CNTs (0.5 wt %) (Hyosung Co., South Korea) were dispersed in isopropyl alcohol. Ultrasonication was performed for 1 h to achieve a uniform dispersion of CNTs. Finally, the CNT-dispersed solution was sprayed onto the MA-patterned PDMS substrate to provide the strain sensor with an active sensing layer.

**Electromechanical Test of the MC Strain Sensor.** The MC strain sensor was characterized by an electromechanical test. For the measurement of resistance, an electrical extension was prepared by applying a silver epoxy at the opposite ends of the strain sensor. The strain sensor was stretched by a tensile tester consisting of a load cell (SM S-type, Interface Inc., USA) and a microactuator (MA-35, Physik Instrumente Inc, USA), measuring the corresponding changes of the resistance using a high-speed LCR meter (E4980A, Keysight Technologies, USA).

**Human Motion Detection Using a Wearable Device-Integrating MC Strain Sensor.** In order to integrate the MC strain sensor to wearable joint bands, the surface of the sensor was protected by a PDMS cap. The MC strain sensor platform was mounted to the center of the commercial joint bands to measure the deformation from a joint flexion−extension of the knee, wrist, ankle, and elbow. A silver epoxy was used for wiring, and sensing output was measured by an LCR meter.

The MC strain sensor was also mounted inside a commercial glove to detect biaxial strains at the backside of the hand and actuate a tendon-driven robot hand. An electrical wiring for measuring sensor signals was formed using a silver epoxy, and interconnection area was encapsulated by PDMS. The resistances of the strain sensor in the two perpendicular directions were measured alternately using Arduino Uno and a switching system realized by three multiplexers (74HC4051, Texas Instruments, USA). Biaxial outputs of the sensor were measured by a voltage-divider circuit, and a servo motor system was prepared for actuating the robot fingers. An external voltage source was provided by a dc power supply (E36312A, Keysight Technologies, USA) for operating the servo motor system. Three servo motors connected to the index, middle, and ring robot fingers were controlled by mapping the $y$-directional (i.e., straightforward direction along the middle finger) responses of the MC strain sensor, and the other two servo motors linked to thumb and little robot fingers were actuated by the $x$-axis direction responses.

## ASSOCIATED CONTENT

### Supporting Information

The Supporting Information is available free of charge at https://pubs.acs.org/doi/10.1021/acs.langmuir.0c01450.

Real-time detection of joint bendingmotion (AVI)

Robot control by detecting biaxial strains under different hand motions (AVI)

Schematic illustration of fabrication processes of an MC strain sensor, sheet resistance of the MC strain sensor



https://dx.doi.org/10.1021/acs.langmuir.0c01450
Langmuir 2020, 36, 8939−8946

varied by the number of spraying of the CNTs, SEM analysis of a long-term reliability of the MC strain sensor, simulation analysis of enhanced Poisson effect of a MA structured elastomer, calculation of SNR of the MC strain sensor, and two-dimensional fitting results of the normalized resistance changes under complex biaxial strains (PDF)

## AUTHOR INFORMATION


### Corresponding Authors

**Yong Suk Oh** − *Department of Mechanical Engineering, Korea Advanced Institute of Science and Technology (KAIST), Daejeon 305-701, South Korea; Center for Bio-Integrated Electronics (CBIE), Northwestern University, Evanston, Illinois 60208, United States*; Email: oyongsuk@kaist.ac.kr

**Inkyu Park** − *Department of Mechanical Engineering, Korea Advanced Institute of Science and Technology (KAIST), Daejeon 305-701, South Korea*; orcid.org/0000-0001-5761-7739; Email: inkyu@kaist.ac.kr

### Authors

**Min Seong Kim** − *Department of Mechanical Engineering, Korea Advanced Institute of Science and Technology (KAIST), Daejeon 305-701, South Korea*

**Kyuyoung Kim** − *Department of Mechanical Engineering, Korea Advanced Institute of Science and Technology (KAIST), Daejeon 305-701, South Korea*

**Donguk Kwon** − *Department of Mechanical Engineering, Korea Advanced Institute of Science and Technology (KAIST), Daejeon 305-701, South Korea*

**Seunghwan Kim** − *Department of Mechanical Engineering, Korea Advanced Institute of Science and Technology (KAIST), Daejeon 305-701, South Korea*

**Jimin Gu** − *Department of Mechanical Engineering, Korea Advanced Institute of Science and Technology (KAIST), Daejeon 305-701, South Korea*

Complete contact information is available at: https://pubs.acs.org/10.1021/acs.langmuir.0c01450


### Author Contributions

The manuscript was written through contributions of all authors. All authors have given approval to the final version of the manuscript.

### Notes

The authors declare no competing financial interest.

## ACKNOWLEDGMENTS

This research was supported by the following research grants: (1) convergence technology development program for bionic arm through the National Research Foundation of Korea (NRF) funded by the Ministry of Science & ICT (no. 2017M3C1B2085318) and (2) the National Research Foundation of Korea (NRF) grant funded by the Korea government (MSIT) (no. 2018R1A2B2004910).

## REFERENCES


(1) Pantelopoulos, A.; Bourbakis, N. G. A Survey on Wearable Sensor-Based Systems for Health Monitoring and Prognosis. *IEEE T. Syst., Man. Cy. C.* **2010**, *40*, 1−12.

(2) Biddiss, E.; Chau, T. Electroactive Polymeric Sensors in Hand Prostheses: Bending Response of an Ionic Polymer Metal Composite. *Med. Eng. Phys.* **2006**, *28*, 568−578.

(3) Gerratt, A. P.; Michaud, H. O.; Lacour, S. P. Elastomeric Electronic Skin for Prosthetic Tactile Sensation. *Adv. Funct. Mater.* **2015**, *25*, 2287−2295.

(4) Shim, B. S.; Chen, W.; Doty, C.; Xu, C.; Kotov, N. A. Smart Electronic Yarns and Wearable Fabrics for Human Biomonitoring Made by Carbon Nanotube Coating with Polyelectrolytes. *Nano Lett.* **2008**, *8*, 4151−4157.

(5) Cherenack, K.; Zysset, C.; Kinkeldei, T.; Münzenrieder, N.; Tröster, G. Woven Electronic Fibers with Sensing and Display Functions for Smart Textiles. *Adv. Mater.* **2010**, *22*, 5178−5182.

(6) Tajima, R.; Kagami, S.; Inaba, M.; Inoue, H. Development of Soft and Distributed Tactile Sensors and the Application to a Humanoid Robot. *Adv. Robotics.* **2002**, *16*, 381−397.

(7) Feliu, V.; García, A.; Somolinos, J. A. Gauge-Based Tip Position Control of a New Three-Degree-of-Freedom Flexible Robot. *Int. J. Robotics Res.* **2001**, *20*, 660−675.

(8) Yamada, T.; Hayamizu, Y.; Yamamoto, Y.; Yomogida, Y.; Izadi-Najafabadi, A.; Futaba, D. N.; Hata, K. A Stretchable Carbon Nanotube Strain Sensor for Human-motion Detection. *Nat. Nanotechnol.* **2011**, *6*, 296−301.

(9) Wang, X.; Gu, Y.; Xiong, Z.; Cui, Z.; Zhang, T. Silk-molded Flexible, Ultrasensitive, and Highly Stable Electronic Skin for Monitoring Human Physiological Signals. *Adv. Mater.* **2014**, *26*, 1336−1342.

(10) Amjadi, M.; Yoon, Y. J.; Park, I. Ultra-stretchable and Skin-mountable Strain Sensors using Carbon Nanotubes-Ecoflex Nanocomposites. *Nanotechnology* **2015**, *26*, 375501.

(11) Turgut, A.; Tuhin, M. O.; Toprakci, O.; Pasquinelli, M. A.; Spontak, R. J.; Toprakci, H. A. K. Thermoplastic Elastomer Systems Containing Carbon Nanofibers as Soft Piezoresistive Sensors. *ACS Omega* **2018**, *3*, 12648−12657.

(12) Gu, J.; Kwon, D.; Ahn, J.; Park, I. Strain Sensor Based on Optical Intensity Change through the Carbon Nanotube Embedded Elastomer. *Proceeding of Transducers 2019 - EUROSENSORS XXXIII*: Berlin, June 2019.

(13) Gu, J.; Kwon, D.; Ahn, J.; Park, I. Wearable Strain Sensors Using Light Transmittance Change of Carbon Nanotube-Embedded Elastomers with Microcracks. *ACS Appl. Mater. Interfaces* **2020**, *12*, 10908−10917.

(14) Wang, Y.; Wang, L.; Yang, T.; Li, X.; Zang, X.; Zhu, M.; Wang, K.; Wu, D.; Zhu, H. Wearable and Highly Sensitive Graphene Strain Sensors for Human Motion Monitoring. *Adv. Funct. Mater.* **2014**, *24*, 4666−4670.

(15) Chun, S.; Choi, Y.; Park, W. All-graphene Strain Sensor on Soft Substrate. *Carbon* **2017**, *116*, 753−759.

(16) Wang, Z.; Zhang, Q.; Yue, Y.; Xu, J.; Xu, W.; Sun, X.; Chen, Y.; Jiang, J.; Liu, Y. 3D Printed Graphene/polydimethylsiloxane Composite for Stretchable Strain Sensor with Tunable Sensitivity. *Nanotechnology* **2019**, *30*, 345501.

(17) Gong, S.; Schwalb, W.; Wang, Y.; Chen, Y.; Tang, Y.; Si, J.; Shirinzadeh, B.; Cheng, W. A Wearable and Highly Sensitive Pressure Sensor with Ultrathin Gold Nanowires. *Nat. Commun.* **2014**, *5*, 3132.

(18) Amjadi, M.; Pichitpajongkit, A.; Lee, S.; Ryu, S.; Park, I. Highly Stretchable and Sensitive Strain Sensor Based on Silver Nanowire-Elastomer Nanocomposite. *ACS Nano* **2014**, *8*, 5154−5163.

(19) Lu, Y.; Jiang, J.; Yoon, S.; Kim, K.-S.; Kim, J.-H.; Park, S.; Kim, S.-H.; Piao, L. High-Performance Stretchable Conductive Composite Fibers from Surface-Modified Silver Nanowires and Thermoplastic Polyurethane by Wet Spinning. *ACS Appl. Mater. Interfaces* **2018**, *10*, 2093−2104.

(20) Zhu, G.-J.; Ren, P.-G.; Guo, H.; Jin, Y.-L.; Yan, D.-X.; Li, Z.-M. Highly Sensitive and Stretchable Polyurethane Fiber Strain Sensors with Embedded Silver Nanowires. *ACS Appl. Mater. Interfaces* **2019**, *11*, 23649−23658.

(21) Pang, C.; Lee, G.-Y.; Kim, T.-I.; Kim, S. M.; Kim, H. N.; Ahn, S.-H.; Suh, K.-Y. A Flexible and Highly Sensitive Strain-gauge Sensor using Reversible Interlocking of Nanofibres. *Nat. Mater.* **2012**, *11*, 795−801.

(22) Lee, J.; Kim, S.; Lee, J.; Yang, D.; Park, B. C.; Ryu, S.; Park, I. A Stretchable Strain Sensor Based on a Metal Nanoparticle Thin Film for Human Motion Detection. *Nanoscale* **2014**, *6*, 11932−11939.
(23) Muth, J. T.; Vogt, D. M.; Truby, R. L.; Mengüç, Y.; Kolesky, D. B.; Wood, R. J.; Lewis, J. A. Embedded 3D Printing of Strain Sensors within Highly Stretchable Elastomers. *Adv. Mater.* **2014**, *26*, 6307−6312.
(24) Zhang, L. M.; He, Y.; Cheng, S.; Sheng, H.; Dai, K.; Zheng, W. J.; Wang, M. X.; Chen, Z. S.; Chen, Y. M.; Suo, Z. Self-Healing, Adhesive, and Highly Stretchable Ionogel as a Strain Sensor for Extremely Large Deformation. *Small* **2019**, *15*, 1804651.
(25) Ryu, S.; Lee, P.; Chou, J. B.; Xu, R.; Zhao, R.; Hart, A. J.; Kim, S.-G. Extremely Elastic Wearable Carbon Nanotube Fiber Strain Sensor for Monitoring of Human Motion. *ACS Nano* **2015**, *9*, 5929−5936.
(26) Kim, K. K.; Hong, S.; Cho, H. M.; Lee, J.; Suh, Y. D.; Ham, J.; Ko, S. H. Highly Sensitive and Stretchable Multidimensional Strain Sensor with Prestrained Anisotropic Metal Nanowire Percolation Networks. *Nano Lett.* **2015**, *15*, 5240−5247.
(27) Lee, J.-I.; Pyo, S.; Kim, M.-O.; Kim, J. Multidirectional Flexible Force Sensors Based on Confined, Self-adjusting Carbon Nanotube Arrays. *Nanotechnology* **2018**, *29*, 055501.
(28) Wang, X.; Li, J.; Song, H.; Huang, H.; Gou, J. Highly Stretchable and Wearable Strain Sensor Based on Printable Carbon Nanotube Layers/Polydimethylsiloxane Composites with Adjustable Sensitivity. *ACS Appl. Mater. Interfaces* **2018**, *10*, 7371−7380.
(29) Lee, H.; Kwon, D.; Cho, J.; Park, I.; Kim, J. Soft Nanocomposite Based Multi-point, Multi-directional Strain Mapping Sensor Using Anisotropic Electrical Impedance Tomography. *Sci. Rep.* **2017**, *7*, 39837.
(30) Legtenberg, R.; Jansen, H.; Boer, M. d.; Elwenspoek, M. Anisotrapic Reactive Ion Etching of Silicon Using $SF_6/O_2/CHF_3$ Gas Mixtures. *J. Electrochem. Soc.* **1995**, *142*, 2020−2027.
(31) Yeo, L. P.; Yan, Y. H.; Lam, Y. C.; Chan-Park, M. B. Design of Experiment for Optimization of Plasma-Polymerized Octafluorocyclobutane Coating on Very High Aspect Ratio Silicon Molds. *Langmuir* **2006**, *22*, 10196−10203.
(32) Song, Y. I.; Yang, C.-M.; Kim, D. Y.; Kanoh, H.; Kaneko, K. Flexible Transparent Conducting Single-wall Carbon Nanotube Film with Network Bridging Method. *J. Colloid Interface Sci.* **2008**, *318*, 365−371.
(33) Wang, S.; Xiao, P.; Liang, Y.; Zhang, J.; Huang, Y.; Wu, S.; Kuo, S.-W.; Chen, T. Network cracks-based wearable strain sensors for subtle and large strain detection of human motions. *J. Mater. Chem. C* **2018**, *6*, 5140−5147.
(34) Wessendorf, A. M.; Newman, D. J. Dynamic Understanding of Human-skin Movement and Strain-field Analysis. *IEEE Trans. Biomed. Eng.* **2012**, *59*, 3432−3438.
(35) Obropta, E. W.; Newman, D. J. A Comparison of Human Skin Strain Fields of the Elbow Joint for Mechanical Counter Pressure Space Suit Development. *IEEE Aerospace Conference*, 2015; pp 1−9.


https://dx.doi.org/10.1021/acs.langmuir.0c01450
*Langmuir* 2020, 36, 8939−8946